

Assessing the robustness of sound horizon-free determinations of the Hubble constant

Tristan L. Smith,¹ Vivian Poulin,² and Théo Simon²

¹*Department of Physics and Astronomy, Swarthmore College, Swarthmore, PA 19081, USA*

²*Laboratoire Univers & Particules de Montpellier (LUPM),*

CNRS & Université de Montpellier (UMR-5299),

Place Eugène Bataillon, F-34095 Montpellier Cedex 05, France

The Hubble tension can be addressed by modifying the sound horizon (r_s) before recombination, triggering interest in early-universe estimates of the Hubble constant, H_0 , independent of r_s . Constraints on H_0 from an r_s -free analysis of the full shape BOSS galaxy power spectra within Λ CDM were recently reported and used to comment on the viability of physics beyond Λ CDM. Here we demonstrate that r_s -free analyses with current data depend on both the model and the priors placed on the cosmological parameters, such that Λ CDM analyses cannot be used as evidence for or against new physics. We find that beyond- Λ CDM models which introduce additional energy density with significant pressure support, such as early dark energy (EDE) or additional neutrino energy density (ΔN_{eff}), lead to larger values of H_0 . On the other hand, models which only affect the time of recombination, such as a varying electron mass (Δm_e), produce H_0 constraints similar to Λ CDM. Using BOSS data, constraints from light element abundances, cosmic microwave background (CMB) lensing, a CMB-based prior on the primordial scalar amplitude (A_s), spectral index (n_s), and Ω_m from the Pantheon+ Type Ia supernovae data set, we find that in Λ CDM, $H_0 = 64.9 \pm 2.2$ km/s/Mpc; in EDE, $H_0 = 68.7_{-3.9}^{+3}$; in ΔN_{eff} , $H_0 = 68.1_{-3.8}^{+2.7}$; and in Δm_e , $H_0 = 64.7_{-2.3}^{+1.9}$. Using a prior on Ω_m from uncalibrated BAO and CMB measurements of the projected sound horizon, these values become in Λ CDM, $H_0 = 68.8_{-2.1}^{+1.8}$; in EDE, $H_0 = 73.7_{-3.9}^{+3.2}$; in ΔN_{eff} , $H_0 = 72.6_{-3.7}^{+2.8}$; and in Δm_e , $H_0 = 68.8 \pm 1.9$. With current data, none of the models are in significant tension with SH_0ES , and consistency tests based on comparing H_0 posteriors with and without r_s marginalization are inconclusive with respect to the viability of beyond Λ CDM models.

I. INTRODUCTION

As cosmological measurements have become more precise they have revealed a few potential issues within the core cosmological model. This model, referred to as ‘ Λ CDM’, consists of a geometrically flat universe filled with baryons, photons, three flavors of neutrinos with the standard weak interactions, cold dark matter (CDM), and a cosmological constant, Λ , with dynamics described by general relativity. The success of this model to describe an exceedingly wide variety of measurements—from light element abundances produced during big bang nucleosynthesis (BBN), to the cosmic microwave background (CMB), to the clustering of galaxies and the more recent expansion history—is remarkable (e.g., Refs. [1, 2]).

These measurements allow for a number of non-trivial consistency tests, the most discerning of which allow us to take observations of the early universe (roughly at or before recombination) and *predict* the values of quantities that are measured in the late universe, within a given model. Interestingly, within Λ CDM applying this to the expansion rate of the universe today, known as the Hubble constant (H_0) and to the current amplitude of the clustering of galaxies, quantified by the standard deviation of the mass contained within spheres with radii equal to $8h^{-1}$ Mpc (σ_8), leads to mismatches between the predicted and directly measured values (known as the ‘Hubble tension’ and ‘ σ_8 tension’, respectfully). Barring the presence of systematic errors affecting multiple, independent measurements (see Refs. [5–9] for discussion), this would indicate that one needs to modify Λ CDM, and in

the process identify new physics that dictate some aspects of the structure and evolution of the universe [10–12].

The statistical significance of these mismatches depends on the particular measurements. However, in all cases the value of H_0 predicted within Λ CDM from measurements of pre-recombination physics (the CMB or the baryon acoustic oscillations—BAO) are smaller than the direct measurements, and in all cases the predicted value of σ_8 is larger (see, e.g., Refs. [5–7, 11, 13–16]). For individual experiments the mismatch for H_0 reaches $\sim 5\sigma$ (between *Planck* and SH_0ES [6, 13]), whereas for σ_8 it is $\sim 3\sigma$ (between *Planck* and KiDS-1000 [15]). Regardless of whether or not these discrepancies are due to physics beyond Λ CDM or yet undiscovered experimental complexities, the increased precision of current cosmological data sets gives us clear motivation to identify additional ways to assess the consistency of Λ CDM.

A fundamentally different type of consistency test focuses on whether a given set of measurements are internally consistent. In the context of CMB measurements, one such approach is to split the data up in multipoles (for the *Planck* satellite the split has been typically taken at $\ell \sim 700 - 800$) and compare the inferred values of the Λ CDM cosmological parameters [17, 18]. Another approach proposes a set of parameters that divides the CMB data into pre- and post-recombination physics [19–22].

Here we focus on tests based on obtaining constraints on H_0 using observations of pre-recombination physics

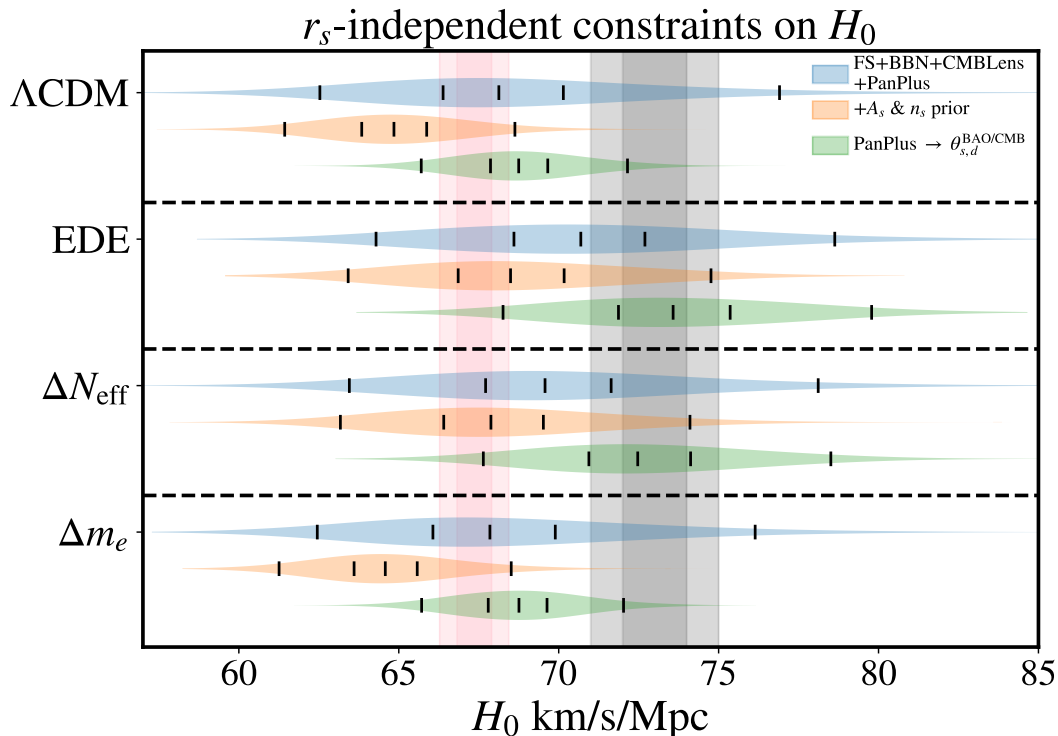


FIG. 1. The 1D posterior distribution for H_0 in the four cosmological models we explore here. The central mark shows the mean of the distributions and the outer marks shows the 68% and 95% confidence level (CL) regions. The gray band indicates the SH_0ES constraint, $H_0 = 73.04 \pm 1.04$ km/s/Mpc [3] and the pink bands the *Planck* value of $H_0 = 67.36 \pm 0.54$ km/s/Mpc [4]. The blue distribution shows the result of an analysis that includes the $r_{s,d}$ -marginalized full-shape of the BOSS DR12 galaxy power spectrum (FS), a BBN prior on the baryon density, the *Planck* CMB lensing potential power spectrum (CMBLens), and a prior on Ω_m from the Pantheon+ Type Ia supernovae data set (PanPlus). The orange distribution shows how constraints shift to lower values when we include a CMB-inspired prior on the scalar amplitude (A_s) and slope (n_s) and the green curves show how they shift back towards larger values when we additionally replace the Ω_m prior from Pantheon+ with one from uncalibrated BAO and CMB measurements of the projected sound horizon ($\theta_{s,d}^{BAO/CMB}$). In all cases the distributions for EDE and ΔN_{eff} are shifted to larger values than in ΛCDM and Δm_e .

with and without information on the sound horizon, r_s .¹ In general, determinations of H_0 rely on a calibrator, usually in the form of a standard ruler (for CMB/BAO) or a standard candle (for Type Ia supernovae, SNeIa), that breaks the degeneracy between the observed angular size/relative flux of an object, and its true distance to us. In fact, the Hubble tension is often described as a tension between calibrators of the distance ladder, which rely either on the Cepheid variable calibration for the absolute magnitude of SNeIa or the ΛCDM value of the sound horizon inferred from CMB data [24, 25]. Consequently, all currently successful attempts to construct ‘beyond’- ΛCDM models to address the Hubble tension propose

¹ The sound horizon is time-dependent and hence there are two different values of the sound horizon that impact cosmological measurements: the sound horizon at recombination, $r_{s,\text{rec}}$, and at baryon decoupling, $r_{s,d}$. The first value is relevant for the CMB and the second for BAO. While the value of either sound horizon can be different in different cosmological models, the difference between them is relatively model-independent with $(r_{s,d} - r_{s,\text{rec}})H_0 \simeq 6 \times 10^{-4}$ [23].

new physics that changes r_s .² A determination of H_0 using observations sensitive to pre-recombination physics which is independent of $r_{s,d}$ (i.e., ‘ r_s -free’) has the potential to provide useful evidence for or against these models [28].

A program of conducting r_s -free analyses using CMB lensing (along with priors on some of the cosmological parameters) has the potential to achieve this goal, but is fundamentally limited by cosmic variance [29]. It is also possible to use measurements of galaxy clustering, along with an effective marginalization over the value of $r_{s,d}$ [28, 30, 31]. Since galaxy surveys have access to a large number of independent modes this has the potential to significantly increase the precision of such an analysis. To do so, one uses the effective field theory (EFT) of large scale structure [32–37] applied to the BOSS DR12 galaxy clustering data (EFT BOSS) [38]. The EFT BOSS data have been shown to allow for determination of the ΛCDM

² We note that it is not possible to address the Hubble tension by modifying the late-time expansion history [26, 27].

parameters at a precision higher than that from conventional BAO and redshift space distortions, as well as to provide interesting constraints on models beyond Λ CDM (see, e.g., Refs. [39–53]).

The way in which r_s -free inferences of H_0 may impact models that attempt to resolve the Hubble tension is two-fold. First, as a predictive test, it could indicate that models which alter r_s to address the Hubble tension are disfavored if the r_s -independent value of H_0 is in tension with direct measurements of H_0 [31]. Second, as an internal consistency test, a comparison between constraints to H_0 with and without $r_{s,d}$ can serve as an indicator for or against beyond- Λ CDM physics [28].

Here we explore whether these analyses provide a robust test of new physics by considering three Λ CDM extensions which affect $r_{s,d}$: an axion-like model of early dark energy (EDE), a model with additional free-streaming ultra-relativistic energy density (ΔN_{eff}), and a model with a value of the electron mass which is different at recombination than it is today (Δm_e). We also investigate how various external priors affect these results. Fig. 1 summarizes the 1D posteriors of H_0 in the $r_{s,d}$ -marginalized analysis for the four models considered in this work.

Using an r_s -free analysis of BOSS DR12, *Planck* CMB lensing, a BBN prior, and Ω_m estimated from Pantheon+ [54], we find that both ΔN_{eff} and EDE open up a new degeneracy between H_0 and the primordial power spectrum (i.e., the scalar amplitude, A_s , and index, n_s) leading to a posterior distribution for H_0 that is shifted to higher values compared to Λ CDM. We find that for all four models we consider, the posterior for H_0 is consistent with the *SH0ES* determination of H_0 at $\sim 1.5\sigma^3$. When imposing an additional CMB-inspired prior on the primordial power spectrum, the inferred value of H_0 in Λ CDM and Δm_e is in tension with *SH0ES* at $\sim 3.5\sigma$, whereas for ΔN_{eff} and EDE the tension drops to 1.7σ and 1.3σ , respectively. As a result we find that, the value of H_0 inferred from an $r_{s,d}$ -marginalized analysis is model dependent. We also find that, as an internal consistency test, with and without $r_{s,d}$ marginalization, the H_0 posteriors are in statistical agreement for all of the models we consider.

This paper is organized as follows. In Sec. II we establish the way in which the various quantities in the r_s -free data depend on Λ CDM parameters. This allows us to anticipate the various degeneracies in a full analysis of these data and establish the role played by A_s and n_s in constraining h . In Sec. III we describe the data sets we use as well as the Markov Chain Monte Carlo (MCMC) analysis we perform. In Sec. IV we establish that within Λ CDM, constraints to h are driven by measurements of the amplitude of the matter power spectrum and constraints to

$\Omega_m h^p$ with $1 \lesssim p \lesssim 2$. In Sec. V we perform r_s -free analyses on three beyond- Λ CDM models. We conclude and discuss the implications of our results in Sec. VI. In Appendix A we give details about how the various data we use depends on cosmological parameters, in Appendix B we demonstrate that the peak of the matter power spectrum does not play a significant role in constraining the Hubble constant, in Appendix C we demonstrate that the broadband/BAO split algorithm works even in cases where the sound horizon deviates significantly from the Λ CDM value, and in Appendix D we show that for the models we consider the full Pantheon+ likelihood is well captured by using a prior on Ω_m .

II. H_0 FROM GALAXY CLUSTERING AND CMB LENSING

To build an intuition as to how h can be constrained without the sound horizon, it is helpful to establish the approximate relationship between the galaxy power spectrum/CMB lensing and the Λ CDM parameters whose values we infer from these data. In this discussion we make the important distinction between how the *amplitude* (i.e., k -independent part) and *shape* (i.e., k -dependent part) of the galaxy power spectrum provides information about the Hubble constant. The work in Refs. [28, 30, 31] emphasizes the role that the shape of the galaxy power spectrum plays— in particular the wavenumber which enters the horizon at matter/radiation equality k_{eq} . Here we show that the amplitude of the $k > k_{\text{eq}}$ part of the galaxy power spectrum also plays an important role in constraining h .

The basic shape of the galaxy power spectrum is set by two main scales: the sound horizon at baryon decoupling

$$r_{s,d} \equiv \int_{z_d}^{\infty} \frac{c_s(z')}{H(z')} dz', \quad (1)$$

where z_d is the redshift at which baryons decouple and $c_s(z)$ is the photon/baryon sound speed (see, e.g., Ref. [55]) and the wavenumber which enters the horizon at matter/radiation equality,

$$k_{\text{eq}} = \frac{\omega_m}{h\sqrt{\omega_r/2}} \frac{100 \text{ hkm/s/Mpc}}{c}, \quad (2)$$

where the last term comes from introducing $h \equiv H_0/(100 \text{ km/s/Mpc})$.

The effects of baryons are imprinted through $r_{s,d}$ and an additional scale, $k_d \equiv H(z_d)/(1+z_d)$, the size of the horizon when baryons decouple from photons and start to fall into the gravitational potentials. The largest effect is a suppression of power at wavenumbers larger than k_d compared to a CDM-only universe. The acoustic oscillations in the baryon/photon fluid (i.e., the BAO) are also imprinted into the galaxy power spectrum as oscillations with a frequency set by integer multiples of $k_{s,d} \equiv 2\pi/r_{s,d}$ [56]. We note that since $k_d < k_{\text{eq}} \simeq 0.01 \text{ hMpc}^{-1}$ this

³ In this paper we quote tension assuming Gaussian posteriors for simplicity. This slightly overestimates the level of tension, due to long tails of distribution, but does not affect our conclusions.

scale is too large to be probed with current galaxy surveys.

The value of k_{eq} plays two important roles in the galaxy power spectrum: it sets the wavenumber at the peak, as well as the range of scales experiencing a logarithmic enhancement in power at $k > k_{\text{eq}}$. In practice, measurements of the galaxy power spectrum cannot probe scales large enough to get a precise measure of the location of the peak [30] (though we note that future HI surveys will be able to measure the peak [57]). For the main analysis presented here we take $k_{\text{min}} = 0.01 h\text{Mpc}^{-1}$ which is just slightly smaller than the typical values of k_{eq} . In Appendix B we also perform an analysis with a larger k_{min} in order to demonstrate that the location of the peak of the galaxy power spectrum does not play a dominant role in constraining h . Because of this, most of the sensitivity to k_{eq} is not in the peak of the galaxy power spectrum, but from the amplitude at scales $k > k_{\text{eq}}$ [30].

Yet, the measurements of h do not only rely on $r_{s,d}$ and k_{eq} , but also on the overall amplitude of the galaxy power spectrum. As discussed in more detail in Appendix A, the galaxy power spectrum amplitude reflects the fact that during radiation domination Hubble friction limits the growth of dark matter perturbations. Once radiation domination ends, the dark matter perturbations grow proportional to the scale factor, a . Therefore, the amplitude of the matter power spectrum scales with $(a/a_{\text{eq}})^2 \propto a^2 \Omega_m^2 h^4$. In this way information about h contained in the amplitude of the galaxy power spectrum provides us with a ‘standard clock’, measuring how much the dark matter perturbations have grown since matter/radiation domination.

Summarizing the results of Appendix A, we can write how the galaxy power spectra and CMB lensing potential power spectrum depend on the amplitude of the primordial power spectrum, A_s , the normalized Hubble constant, h , the ‘geometric’ matter density, Ω_m , and the physical radiation energy density, $\omega_r \equiv \Omega_r h^2$. Note that all measured quantities are dimensionless, so in the following equations lengths are written in h^{-1} Mpc.

The overall amplitudes of the galaxy power spectrum, P_{gal} , and the CMB lensing power spectrum, $C_L^{\phi\phi}$, scale as

$$P_{\text{gal}} \propto b^2 R_c^2 A_s \Omega_m^{2.25} \omega_r^{-2} h^4, \quad (3)$$

$$L^4 C_L^{\phi\phi} \propto A_s \Omega_m^{3.5} \omega_r^{-1} h^{2.6}, \quad (4)$$

where b is the linear bias, $R_c \equiv \omega_{\text{cdm}}/\omega_m = 1 - \omega_b/\omega_m$ is the baryon suppression [58], and ω_{cdm} is the physical cold dark matter density today. It is interesting to note that, while these are all proportional to A_s , they depend on different powers of h indicating that the combination of P_{gal} and $C_L^{\phi\phi}$ can break the $A_s - h$ degeneracy. It is also evident that additional information on Ω_m will further help constraining h .

The shape of these power spectra depend on

$$\left(\frac{k}{k_p/h}\right)^{n_s-1} = \left(\frac{k}{(0.05/h) h\text{Mpc}^{-1}}\right)^{n_s-1}, \quad (5)$$

$$k_{\text{eq}}/h \propto \Omega_m \omega_r^{-0.5} h, \quad (6)$$

$$\ell_{\text{peak}}^{\phi\phi} \propto \Omega_m^{0.75} \omega_r^{-0.5} h, \quad (7)$$

where n_s is the primordial scalar spectral index and $k_p = 0.05 \text{Mpc}^{-1}$ is the standard pivot scale [55]. Note that the different Ω_m scalings provide a way to break the degeneracy between Ω_m and h . Moreover, the baryon suppression and amplitude of the BAO in the galaxy power spectrum gives information about the ratio ω_b/ω_m . Finally, redshift space distortions provide additional sensitivity to

$$f\sigma_8 \propto A_s^{1/2} \Omega_m^{1.25} \omega_r^{-0.65} h^{1.75}, \quad (8)$$

where f is the growth rate and σ_8^2 is the variance of the fractional mass fluctuations in spheres of comoving radius $R = 8h^{-1} \text{Mpc}$.

These scaling equations allow us to understand general trends in the posterior distributions. First, as it was noted before, it is clear that knowledge of $k_{\text{eq}} \propto \Omega_m h$ and Ω_m from, e.g. SNeIa, provides a constraint on h [30]. In fact, the whole shape of the power spectra, through k_{eq} , baryon suppression, and $\ell_{\text{peak}}^{\phi\phi}$, provides constraints to $\Omega_m h^p$, where $1 \lesssim p \lesssim 2$. Yet, these are not the only parameters appearing in this scaling: A_s and n_s also play an important role. For example, in ΛCDM ω_r is fixed and with a Pantheon+ prior on Ω_m , Eqs. (3), (4) and (8) show that an increase in h must be accompanied by a decrease in A_s in order to keep the amplitudes unaffected. This additional degeneracy will be even more important for beyond ΛCDM determinations of h .

III. COSMOLOGICAL MODELS AND DATA ANALYSIS

In order to explore the extent to which an r_s -free analysis may depend on the cosmological model, we consider three beyond- ΛCDM models that affect the value of the sound horizon in different ways.

The sound horizon is inversely proportional to the Hubble parameter before recombination [see Eq. (1)]. We consider two models which lead to changes in the early-universe Hubble parameter: variations in the number of ultra-relativistic neutrinos, ΔN_{eff} (we always take one neutrino to have a mass of 0.06 eV), and the ultra-light axion-inspired model for EDE [59, 60] (we use the scalar field potential $V = m^2 f^2 [1 - \cos(\phi/f)]^3$, where m is the axion mass, f is the axion decay constant and ϕ the field value). As described in Ref. [60], we use a shooting method to map the set of phenomenological parameters $\{\log_{10}(z_c), f_{\text{EDE}}(z_c)\}$ (which describe when the field becomes dynamical and its maximum fractional contribution to the total energy density, respectively) to the

theory parameters $\{m, f\}$. A major difference between these two ‘energy density modification’ models is that while a change to the neutrino energy density has an impact throughout radiation domination, the EDE’s energy density makes a dynamically relevant contribution to the total energy density over a relatively short period of time.

The sound horizon depends on the redshift at which baryons decouple from photons, z_d [see Eq. (1)]. We also consider a model in which the mass of the electron may be different around recombination than its value today, leading to a change in the Thomson scattering cross section, and hence changing z_d (see, e.g., Refs. [61, 62]).

Our Markov-Chain Monte Carlo (MCMC) analyses uses `MontePython-v3`⁴ code [20, 63] interfaced with modified versions of `CLASS-PT`⁵ which is itself a modified version of `CLASS`⁶ [64].

In this paper, we carry out various analyses using a combination of the following data sets:

- **Full-shape galaxy power spectra (FS):** The effective field theory (EFT) of large scale structure applied to the BOSS DR12 galaxy clustering data. For the main analysis we use the same data and code as in Ref. [31]: we use the power spectrum measured in Ref. [47] from the $z = 0.38$ and 0.61 redshift bins at the Northern and Southern Galactic Caps [65]. We use the unreconstructed monopole, quadrupole, and hexadecapole galaxy power spectrum multipoles with⁷ $0.01h \text{ Mpc}^{-1} \leq k \leq 0.2h \text{ Mpc}^{-1}$ and the real-space extension, Q_0 , with $0.2 h\text{Mpc}^{-1} \leq k \leq 0.4 h\text{Mpc}^{-1}$. We include EFT parameters and priors as described in Refs. [47, 66]. Note that these priors were shown to be informative, and part of our results could be affected by the choice of priors, at the 1σ level [66], but we do not expect our main conclusions to change.
- **BBN:** The BBN measurement of ω_b [67] that uses the theoretical prediction of [68], the experimental Deuterium fraction of [69] and the experimental Helium fraction of [70]. Note that this likelihood also tightly constrains ΔN_{eff} [67]. As we are interested in computing constraints driven by galaxy clustering/CMB lensing, when varying ΔN_{eff} we instead use a Gaussian prior on $\omega_b = 0.02268 \pm 0.00038$ [40].
- **CMB lensing (CMBLens):** The CMB-marginalized gravitational lensing potential from *Planck* 2018 temperature and polarization data with $8 \leq L \leq 400$ [71].

- **Pantheon+ (PanPlus):** The Pantheon+ measurement of $\Omega_m = 0.338 \pm 0.018$ using uncalibrated Type Ia supernovae (SNIa), modeled as a Gaussian likelihood [54]. We have explicitly checked that this prior captures all of the information contained within the full likelihood in Appendix D.

- **Uncalibrated BAO and CMB measurements of the projected sound horizon ($\theta_{s,d}^{\text{BAO/CMB}}$):** In some of our analyses we have replaced the Ω_m prior from PanPlus with one from an analysis of uncalibrated BAO measurements of $r_{s,d}H(z)$ and $\theta_{s,d}(z) = r_{s,d}/D_A(z)$ and the *Planck* inferred value of $100\theta_{s,d}(z_{\text{CMB}})$, $\Omega_m = 0.30 \pm 0.01$ [23]. We have taken the uncertainty to be 25% larger in order to account for variations in $\theta_{s,d}(z_{\text{CMB}})$ when fit to the cosmological models we consider. We note that some of the data used to generate this prior is correlated with the FS data, but stress that our use of this prior is primarily meant to highlight how constraints on Ω_m affect the r_s -free results.

- **CMB priors:** For some of our analyses we use the Gaussian priors $\ln 10^{10} A_s = 3.044 \pm 0.08$ and $n_s = 0.96 \pm 0.03$. The prior on A_s is 8% around the *Planck* mean value [29, 31] and the prior on n_s is based on the one used in Ref. [31], but is lightly wider in order to account for the fact that some of the beyond- Λ CDM models we consider, when fit to the CMB, lead to larger values for n_s (see, e.g. Refs. [60, 72, 73]).

In the following we denote the combination of FS, BBN, CMBLens, and PanPlus as ‘All’, to distinguish it from analyses that just combine a subset of these data sets.

All MCMCs use wide uninformative flat priors on the physical CDM energy density, ω_{cdm} , the Hubble parameter today in units of 100km/s/Mpc , h , the logarithm of the variance of curvature perturbations centered around the pivot scale $k_p = 0.05 \text{ Mpc}^{-1}$ (according to the *Planck* convention [55]), $\ln 10^{10} A_s$, and the scalar spectral index n_s .

We marginalize over information about the sound horizon in the galaxy power spectra following the procedure introduced in Ref. [28]. This involves splitting the linear power spectrum into its broadband (BB) shape and the BAO and marginalizing over a new scaling parameter, α_{r_s} ,

$$P_{\text{lin}}(k) = P_{\text{BB}}(k) + P_{\text{BAO}}(\alpha_{r_s} k). \quad (9)$$

As with the cosmological parameters, we use a wide uninformative flat prior on α_{r_s} . We note that Ref. [31] places a Gaussian prior with mean equal to 1 and a standard deviation of 0.5. Since the value of α_{r_s} only varies by ~ 0.1 their choice of prior is also uninformative.

For the three free parameters of the EDE model, we impose a logarithmic priors on z_c , and flat priors for

⁴ https://github.com/brinckmann/montepython_public

⁵ <https://github.com/Michalychforever/CLASS-PT>

⁶ https://lesgourg.github.io/class_public/class.html

⁷ For one part of our analysis we increase the minimum k to $0.05 h\text{Mpc}^{-1}$ for the galaxy power spectrum multipoles.

Parameter	Λ CDM (no $r_{s,d}$ -marg)	Λ CDM ($r_{s,d}$ -marg)
$10^2 \omega_b$	2.273 ± 0.038	2.273 ± 0.037
ω_{cdm}	$0.1395^{+0.0091}_{-0.012}$	$0.137^{+0.011}_{-0.022}$
Ω_m	0.335 ± 0.013	0.340 ± 0.015
h	$0.697^{+0.014}_{-0.016}$	$0.687^{+0.030}_{-0.050}$
$\ln 10^{10} A_s$	2.839 ± 0.096	$2.86^{+0.16}_{-0.13}$
n_s	0.853 ± 0.052	$0.863^{+0.081}_{-0.060}$
$r_{s,d}$ [Mpc]	$141.9^{+2.7}_{-2.4}$	$142.7^{+5.1}_{-3.2}$
α_{r_s}	–	$1.011^{+0.036}_{-0.028}$

TABLE I. The mean and $\pm 1\sigma$ uncertainties of the Λ CDM cosmological parameters with and without marginalization over $r_{s,d}$ and using ‘All’ of the data.

$f_{\text{EDE}}(z_c)$ and θ_i :

$$\begin{aligned} 3 &\leq \log_{10}(z_c) \leq 4, \\ 0 &\leq f_{\text{EDE}}(z_c) \leq 0.5, \\ 0 &\leq \theta_i \equiv \phi_i/f \leq 3.1. \end{aligned}$$

When we vary the electron mass we use the prior $0.8 \leq m_e/m_{e,0} \leq 1.2$, while we take $\Delta N_{\text{eff}} \geq 0$ when we vary the amount of free-streaming ultra-relativistic energy density. We define our MCMC chains to be converged when the Gelman-Rubin criterion $R - 1 < 0.05$ [74]. Finally, we produce our figures using `GetDist` [75].

IV. CONSTRAINTS ON h IN Λ CDM

We start by comparing the 1D posterior distributions of h from analyzing FS+BBN+CMBLens+PanPlus (the ‘All’ dataset), with and without marginalizing over $r_{s,d}$, without applying any CMB priors on A_s or n_s . The Λ CDM posterior distributions are summarized in Tab. I, and we find:

$$\begin{aligned} h &= 0.697^{+0.014}_{-0.016} \text{ w/o } r_{s,d}\text{-marg.}, \\ h &= 0.687^{+0.030}_{-0.050} \text{ w/ } r_{s,d}\text{-marg.} \end{aligned}$$

which shows no significant tension with $SH_0\text{ES}$ even when marginalizing over $r_{s,d}$. We note that, as shown in Table I the mean value of $r_{s,d}$ is ~ 5 Mpc smaller than the value preferred by *Planck* [4]. This is due to the fact that these data prefer a significantly larger mean physical CDM density, $\omega_{cdm} \sim 0.14$, compared to *Planck*, $\omega_{cdm} \sim 0.12$. The larger ω_{cdm} , combined with the relatively large value of Ω_m from PanPlus, leads to the statistical agreement between constraints to h from the two datasets. We also note that we find no significant shift between the two values of h , which has been advocated as being a hint against the presence of new physics affecting the sound horizon [31, 47]. This $r_{s,d}$ -marginalized value is larger than the main value reported in Ref. [31] because here we have not imposed any external priors on

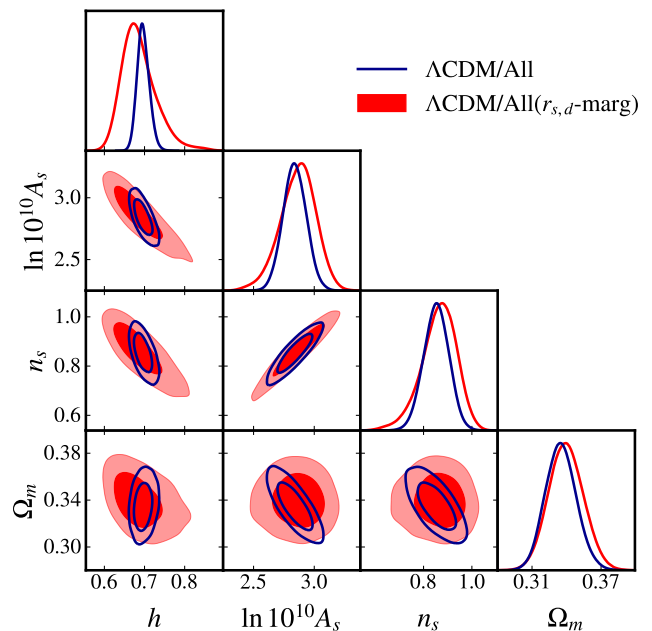


FIG. 2. A triangle plot showing the constraints to four of the five Λ CDM cosmological parameters with and without marginalization over $r_{s,d}$ (we do not show the posterior distribution for ω_b since it is well constrained by the BBN likelihood). The filled contours show constraints using ‘All’ of the data without marginalization over $r_{s,d}$ whereas the unfilled contours show the same data with marginalization over $r_{s,d}$.

n_s or A_s .⁸ As shown in Table I, both A_s and n_s are lower than what is found using CMB data, and when imposing priors from the CMB the posterior on h can change appreciably. In Sec. IV A we explore the degeneracy between h and A_s/n_s and in Sec. IV B we show the impact of imposing the CMB priors.

A. The A_s/n_s -degeneracy

To understand the role that the FS galaxy power spectra are playing in constraining h , Fig. 2 shows a comparison between two different data analyses: FS+BBN+CMBLens+PanPlus with and without $r_{s,d}$ -marginalization. First, focusing on the constraints to h (left-most column) and on the analysis without $r_{s,d}$ -marginalization one can see that the constraint on h is less degenerate with A_s , n_s , and Ω_m than with $r_{s,d}$ -marginalization. This shows that when including information on $r_{s,d}$ one gains independent information on h

⁸ Ref. [31] argues that their results are robust to dropping any priors on n_s or A_s , in this case reporting $h = 0.660^{+0.027}_{-0.034}$. However, even after adopting the same parameter settings as they use, without these priors we find $h = 0.677^{+0.028}_{-0.037}$, giving posterior on h that is consistent with the $SH_0\text{ES}$ value at $\sim 2\sigma$.

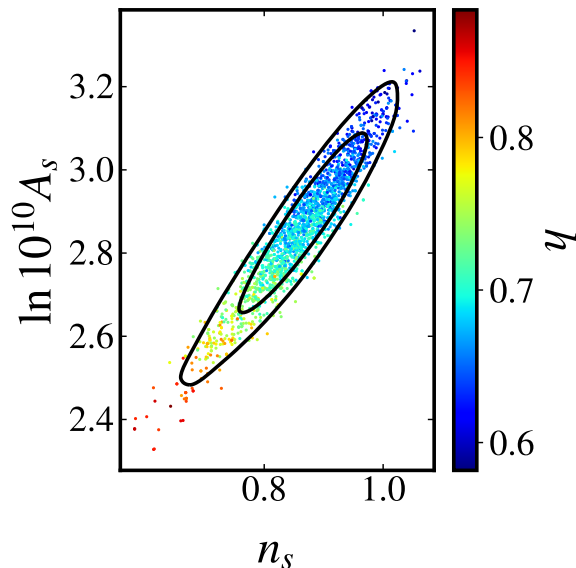


FIG. 3. The 3D correlation between n_s , $\ln 10^{10} A_s$, and h for an $r_{s,d}$ -marginalized analysis of Λ CDM using ‘All’ of the data. We can see that h has a strong negative correlation with both A_s and n_s .

through its effect on the projected size of the sound horizon. When marginalizing over $r_{s,d}$ on the other hand, one can see that h is anti-correlated with A_s/Ω_m , as expected from the discussion in Sec. II. In particular the degeneracy between h and A_s provides evidence that constraints on h when marginalizing over $r_{s,d}$, at least in part, come from the amplitude of the galaxy power spectrum.

Fig. 2 clearly shows that when marginalizing over $r_{s,d}$, h and n_s are anti-correlated. This anticorrelation is also related to the primordial amplitude of the fluctuations which can be seen in the 3D plot in Fig. 3. There we can see that a decrease in n_s is compensated by a decrease in A_s and an increase in h . This relationship is due to a balance between the enhancement of power for $k > k_p = 0.05/h \text{ hMpc}^{-1}$ (for $n_s < 1$) and the shift with h in scale at which the logarithmic enhancement starts, $k_{\text{eq}} = \Omega_m h$.

We further explore the exact shape of the degeneracies introduced through the amplitudes of the $k > k_{\text{eq}}$ galaxy power spectra and the CMB lensing potential power spectrum as discussed in Sec. II and Appendix A. The top left panel of Fig. 4 shows the results of using FS + BBN. The dashed red curves show the mean and $\pm 1\sigma$ of $A_s \Omega_m^{2.25} h^4$, which sets the $k > k_{\text{eq}}$ amplitude of the galaxy power spectrum [see Eq. (3)]. The agreement between the red curves and the 2D posterior definitively demonstrates the importance of the $k > k_{\text{eq}}$ amplitude of the galaxy power spectrum in constraining h with these data.

The bottom left panel of Fig. 4 shows the same curve/2D posteriors but with FS+BBN+CMBLens. There we can see that the addition of CMB lensing data shifts the h vs. $A_s \Omega_m^{2.25}$ contour, and decreases the width

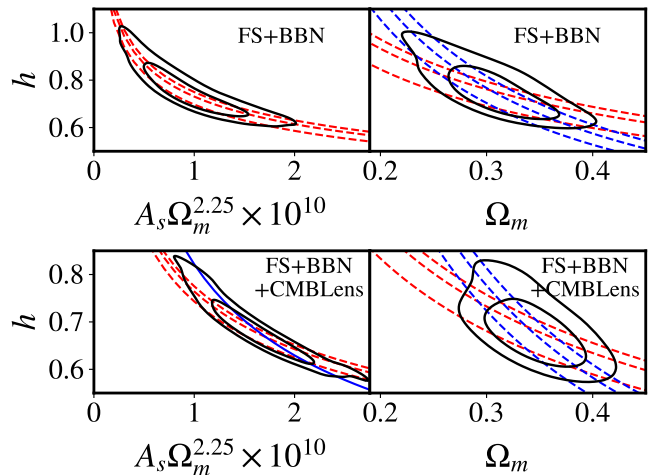


FIG. 4. A pair of 2D posteriors comparing r_s -marginalized constraints using FS + BBN (top row) vs. FS+BBN+CMBLens. The red curves in the two left panels show the mean and $\pm 1\sigma$ values for $A_s \Omega_m^{2.25} h^4$, which captures information in the small-scale ($k > k_{\text{eq}}$) part of the galaxy power spectrum [see Eq. (3)]. The solid blue curve in the bottom left panel corresponds to the $\propto h^{2.6}$ scaling from the lensing data [see Eq. (4)]. The red/blue curves in the right panels show the mean and $\pm 1\sigma$ for $\omega_m = \Omega_m h^2$ and $k_{\text{eq}} = \Omega_m h$, respectively. The agreement between the curves and the contours indicates that both the small-scale amplitude and the various combinations of $\Omega_m h^p$ (characterizing the shape of the power spectra), with $1 \lesssim p \lesssim 2$, plays a role in constraining h .

of the posterior, indicating that CMB lensing adds information on h . The blue curve in this panel shows the $\propto h^{2.6}$ scaling from the amplitude of the lensing potential power spectrum [see Eq. (4)]. Its shape at least partially explains the shift in this parameter plane when the lensing is included.

B. The impact of priors on n_s and A_s in constraining h in Λ CDM

Given the correlation between h and A_s/n_s , it is of interest to consider how placing priors on the primordial power spectrum affects h . Ref. [31] imposed $n_s = 0.96 \pm 0.02$ or an 8% prior on A_s centered on the *Planck* value, $\ln 10^{10} A_s = 3.044 \pm 0.08$. Since here we consider both Λ CDM and beyond- Λ CDM models which prefer larger values of n_s when fit to CMB data [60, 72, 73], we use the same prior on A_s but a slightly wider prior for $n_s = 0.96 \pm 0.03$. We find good agreement with Ref. [31] when imposing the same priors, and the specific choice of priors do not affect our overall conclusions.

When imposing both A_s and n_s priors, we find that the resulting posterior on h decreases from $h = 0.687_{-0.05}^{+0.03}$ to $h = 0.649 \pm 0.022$. This significant downward shift is not surprising, given that h is anti-correlated with both

A_s and n_s as discussed above, and that these priors are larger than the values preferred by ‘All’ of the data (see Fig. 2 and 3). When imposing these priors, we find that the value of h is in 3.3σ tension with SH_0ES . The tension level is slightly stronger than that reported in Ref. [31] because we impose both priors at the same time.

C. The role of Ω_m in constraining h

The scaling equations discussed in Sec. II and the right-hand contours in Fig. 4, indicate that the shape of both the FS data and the CMB lensing potential power spectrum constrain various combinations of $\Omega_m h^p$, where $1 \lesssim p \lesssim 2$. These constraints, along with a prior on Ω_m , provides a constraint on h .

The red/blue dashed curves in the top right panel shows the mean and $\pm 1\sigma$ of $\omega_m = \Omega_m h^2$ and $\Omega_m h$, respectively. The rough agreement indicates that some combination of $\Omega_m h^p$, with $1 \lesssim p \lesssim 2$, plays a role in constraining h . Since the $\Omega_m h^p$ constraint comes from several aspects of the measurements with slightly different dependencies– baryonic effects ($\Omega_m h^2$), the logarithmic enhancement of the $k > k_{\text{eq}}$ part of the galaxy power spectrum ($\Omega_m h$), the peak of the lensing potential power spectrum ($\Omega_m h^{1.33}$)– we expect the degeneracy between h and Ω_m to be less well-defined. The bottom right panel shows that, as with FS+BBN, some combination of $\Omega_m h^p$, with $1 \lesssim p \lesssim 2$, continues to play a role in constraining h in the FS+BBN+CMBLens analysis.

These scaling equations indicate that if the prior on Ω_m decreases then the inferred value of h will increase. So far we have used a prior on Ω_m from PanPlus: $\Omega_m = 0.338 \pm 0.018$ [54]. This value is $\sim 2\sigma$ larger than the value of Ω_m inferred from the uncalibrated BAO and CMB measurements of the projected sound horizon: $\Omega_m = 0.3 \pm 0.01$ [23].

Replacing the PanPlus prior on Ω_m with the BAO/CMB angular prior allows us to explore how information about Ω_m impacts the $r_{s,d}$ -marginalized ΛCDM posterior on h . As expected with the lower Ω_m the mean value of h increases from $h = 0.687_{-0.050}^{+0.030}$ to $h = 0.734_{-0.063}^{+0.033}$. This demonstrates that at least part of the apparent tension in ΛCDM with SH_0ES comes from the relatively high value of Ω_m favored by Pantheon+. If we also impose the A_s/n_s prior then the posterior distribution for h increases from $h = 0.649 \pm 0.022$ to $h = 0.688_{-0.021}^{+0.018}$. With the A_s/n_s prior we can see that the change in the Ω_m prior leads to a 1.3σ shift in the mean of h .

V. CONSTRAINTS IN BEYOND- ΛCDM MODELS

We first establish that without marginalizing over $r_{s,d}$ the three beyond- ΛCDM models that we consider have the expected effect on the value of $r_{s,d}$.

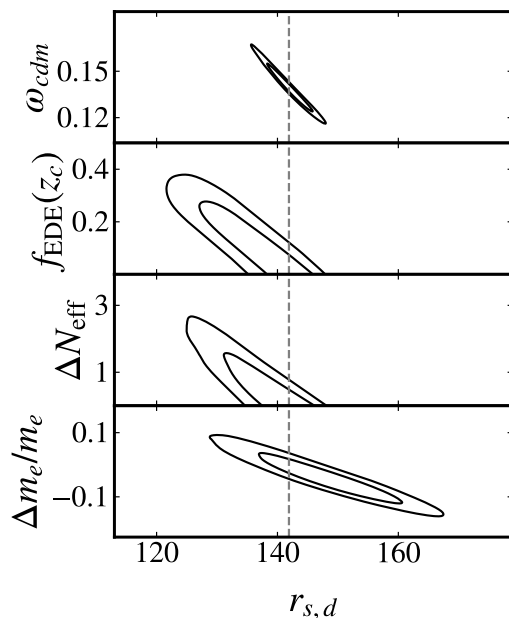


FIG. 5. The 2D posterior distribution for ΛCDM and the three beyond- ΛCDM models we consider using ‘All’ of the data (without marginalizing over $r_{s,d}$). The dashed gray line is the mean value for ΛCDM . We can see that as the beyond- ΛCDM model parameters vary the inferred value of $r_{s,d}$ varies, as expected.

Fig. 5 shows that the three beyond- ΛCDM models affect $r_{s,d}$ as expected. In particular, $f_{\text{EDE}}(z_c)$ – which controls the maximum contribution that the EDE field makes to the total energy density– is only able to *increase* the pre-recombination value of H , and therefore it can only lead to a *decrease* in $r_{s,d}$. Variations in the number of massless neutrinos, $\Delta N_{\text{eff}} > 0$, can only cause a decrease in $r_{s,d}$ from its ΛCDM value (shown by the vertical dashed line). The Thomson scattering cross-section scales as $1/m_e^2$, so a larger electron mass leads to a decrease in the scattering rate, which in turn causes the baryons to decouple earlier than they would have. Therefore as m_e increases, z_d increases, leading to a decrease in $r_{s,d}$ (see Eq. 1).

A. r_s -marginalized constraints on H_0 beyond ΛCDM

We provide the marginalized constraints on h for ΛCDM and the three beyond- ΛCDM models we consider in Table II.

The oscillation frequency of the BAO is equal to $r_{s,d}$. Since we marginalize over the product $\alpha_{r_s} k$ within the BAO, and observations are in angular/redshift space, the directly measured quantity is $\alpha_{r_s} h r_{s,d}$, and therefore should be relatively stable between the different models we have analyzed. In Fig. 6 we show that for the three cosmological models we analyze, this combination is rel-

	Λ CDM	EDE	ΔN_{eff}	Δm_e
w/o $r_{s,d}$ marg	$0.697^{+0.014}_{-0.016}$	$0.736^{+0.027}_{-0.036}$	$0.724^{+0.021}_{-0.030}$	$0.671^{+0.031}_{-0.040}$
with $r_{s,d}$ marg	$0.687^{+0.030}_{-0.050}$	$0.708^{+0.038}_{-0.049}$	$0.699^{+0.034}_{-0.050}$	$0.684^{+0.031}_{-0.049}$
PanPlus $\rightarrow \theta_{s,d}^{\text{BAO/CMB}}$	$0.734^{+0.033}_{-0.063}$	$0.748^{+0.038}_{-0.046}$	$0.739^{+0.035}_{-0.052}$	$0.716^{+0.032}_{-0.038}$
+ A_s & n_s prior	0.649 ± 0.022	$0.687^{+0.030}_{-0.039}$	$0.681^{+0.027}_{-0.038}$	$0.647^{+0.019}_{-0.023}$
PanPlus $\rightarrow \theta_{s,d}^{\text{BAO/CMB}}$	$0.688^{+0.018}_{-0.021}$	$0.737^{+0.032}_{-0.039}$	$0.726^{+0.028}_{-0.037}$	0.688 ± 0.019

TABLE II. The mean and $\pm 1\sigma$ uncertainties of h in the four models we explore. The ‘PanPlus’ prior is $\Omega_m = 0.338 \pm 0.018$ and the uncalibrated BAO and CMB measurements of the projected sound horizon, $\theta_{s,d}^{\text{BAO/CMB}}$, prior is $\Omega_m = 0.3 \pm 0.01$. When we replace the Ω_m prior we apply it to the analysis described in the above row.

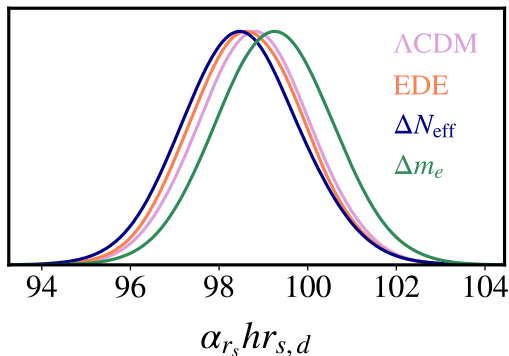


FIG. 6. When marginalizing over $r_{s,d}$ we are effectively measuring the product $\alpha_{r_s} h r_{s,d}$. Here we can see that all four cosmological models produce statistically identical posterior distributions for this product when using ‘All’ of the data.

atively unchanged, as expected. This provides evidence that our marginalization over α_{r_s} is correct even in these extended cosmologies. This is discussed further in Appendix C.

The main result of this section is shown in Fig. 7. There we can see how both ΔN_{eff} and EDE produce similar posteriors in the h vs. $\ln 10^{10} A_s/n_s$ plane, whereas the varying m_e model is qualitatively different, and similar to what we obtain in Λ CDM (shown in the brown contour in the bottom plot). The color bars of Fig. 7 show that the larger values of ΔN_{eff} and $f_{\text{EDE}}(z_c)$ open up a new degeneracy, allowing for a simultaneous increase in h , A_s , and n_s . This is due to the fact that unlike Δm_e , both EDE and ΔN_{eff} introduce additional energy density with significant pressure support. This leads to a suppression of the growth of matter perturbations, leading to a degeneracy with the primordial power spectrum—i.e., A_s and n_s —for these models, allowing these parameters to take on larger values than they do in Λ CDM and Δm_e .

One can see how this increase in parameter space affects the 1D marginalized posterior distribution for h in Fig. 8. Without marginalizing over $r_{s,d}$ (top panel) the posterior distribution for h varies significantly between the different models. When marginalizing over $r_{s,d}$ both EDE and ΔN_{eff} are shifted to larger values of h than Λ CDM and Δm_e . It is also clear that EDE opens up

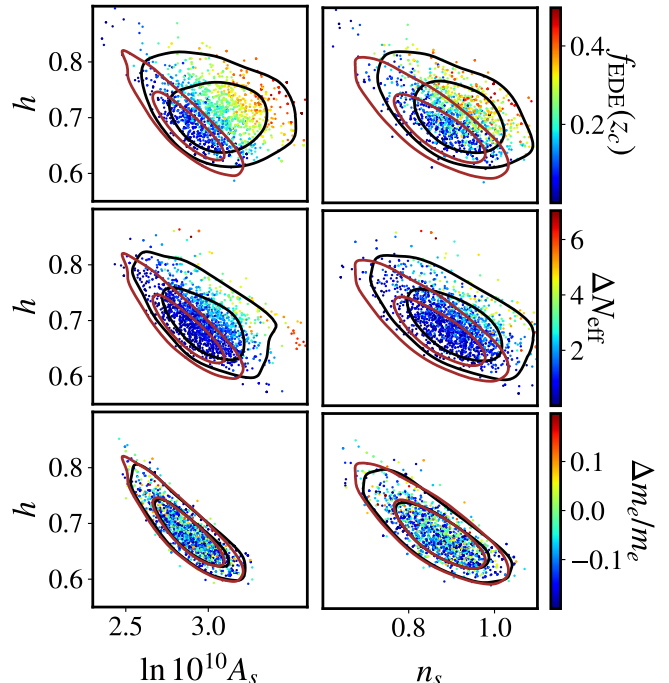


FIG. 7. The h vs. $\ln 10^{10} A_s$ and h vs. n_s 2D posterior distributions for the three beyond- Λ CDM models we consider from the r_s -marginalized analyses. The brown contours show the Λ CDM constraints. In EDE and ΔN_{eff} we can see that additional parameter space is opened which allows for a larger value of h at larger values of A_s with a corresponding increase in the model parameter (shown in the color bars). On the other hand, when varying m_e , we obtain contours statistically identical to Λ CDM.

more parameter space volume than ΔN_{eff} . An important distinction between the physics of these two models is that the additional neutrino energy density has an effect throughout radiation domination whereas the additional energy density in EDE is only briefly relevant. This leads to a different scale dependence of their effects and different degeneracies with A_s and n_s , which allows EDE to achieve a larger posterior for A_s and n_s , as shown in Fig. 9, with larger values of A_s/n_s corresponding to smaller values of $\log_{10} z_c$.

We note that even if the EDE/ ΔN_{eff} posteriors for h were not shifted to larger values, the width of all of the h

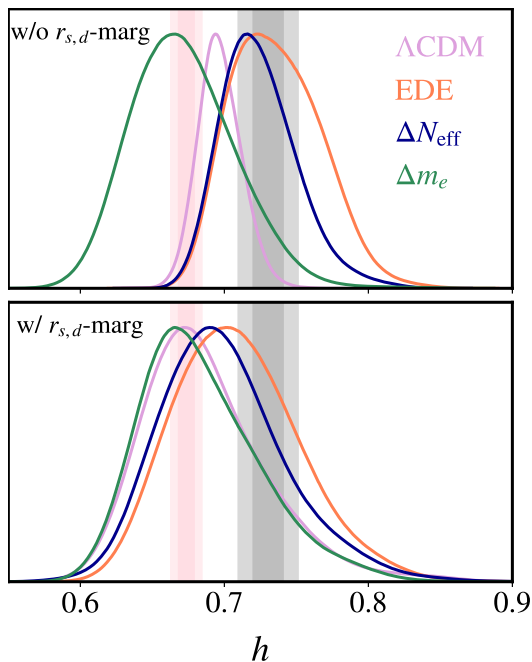


FIG. 8. The 1D posterior distribution for h without (top) and with (bottom) marginalizing over $r_{s,d}$. The top panel shows that the inferred value of h , which is dominated by information about the sound horizon, varies between the four cosmological models. When marginalizing over $r_{s,d}$ the posteriors become similar, with EDE shifted to a slightly larger value of h . The gray bands indicate the SH_0ES value of $h = 0.73 \pm 0.01$ and the pink bands the *Planck* value of $h = 0.6736 \pm 0.0054$.

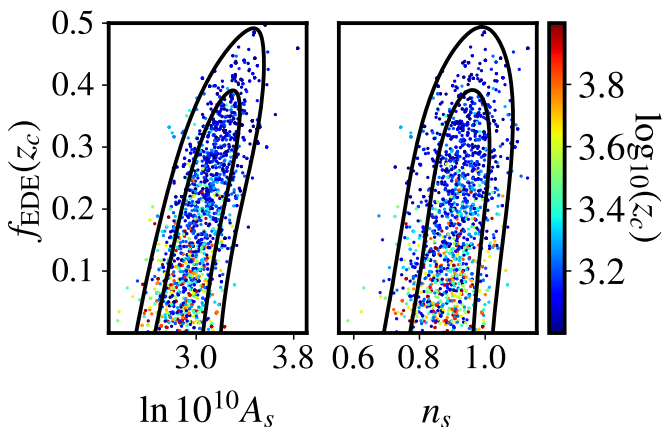


FIG. 9. The 2D posterior distribution for A_s and n_s vs. $f_{EDE}(z_c)$ from the r_s -marginalized analysis. We can see that the largest values of n_s and A_s in EDE occur when z_c is at the lower end of its prior range. This additional parameter allows EDE to achieve a 1D posterior distribution for h that is slightly larger than in ΔN_{eff} .

posteriors can easily account for the *Planck* and SH_0ES -inferred values. As such, none of these analysis rule out these models as resolutions to the Hubble tension.

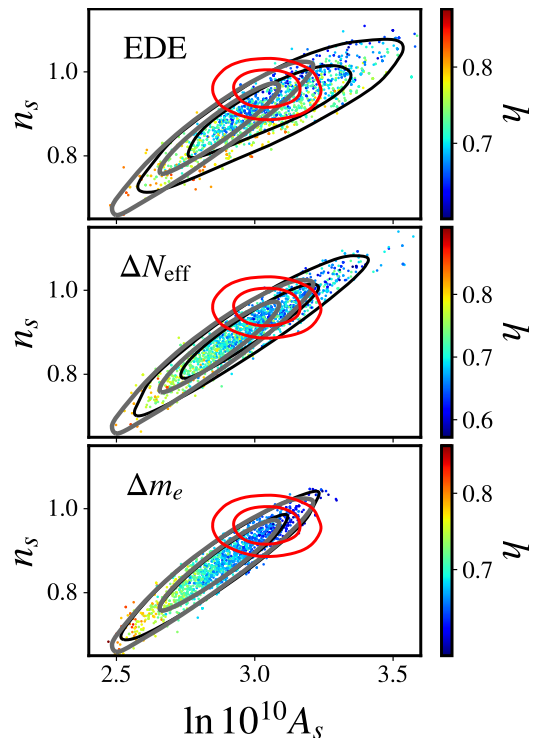


FIG. 10. The 3D posterior distribution for ‘All’ of the data (from the r_s -marginalized analysis) in the n_s vs. $\ln 10^{10} A_s$ plane along with color coded points indicating the corresponding value of h for the three beyond- ΛCDM models we explore. The gray contours show the results in ΛCDM , the red contours show the CMB priors we place on A_s and n_s .

B. Impact of n_s and A_s priors

Just as in ΛCDM , given the negative degeneracy between A_s/n_s and h in an r_s -free analysis (see Fig. 7) any priors on these parameters will lead to a significant change in the 1D posterior distribution for h . The result of including a CMB prior on A_s and n_s is shown in the second from the bottom row of Table II. There we can see that the degeneracies introduced by EDE and ΔN_{eff} lead to a $\sim 1\sigma$ shift in h to higher values compared to ΛCDM and Δm_e .

We can better understand how the A_s and n_s prior affects these analysis by examining Fig. 10. There we show the 3D posterior for n_s , $\ln 10^{10} A_s$, and h . The gray contour shows the n_s vs. $\ln 10^{10} A_s$ posterior distribution in ΛCDM and the red contour shows the CMB prior on A_s and n_s . The EDE and ΔN_{eff} panels clearly show that these models open new parameter space to allow for larger values of A_s and n_s at correspondingly larger values of h . When placing a prior on A_s and n_s this additional volume leads to a 1D posterior distribution for h which is shifted to larger values (i.e., cyan and yellow points) than in Δm_e or ΛCDM .

C. Impact of the Ω_m priors

Replacing the PanPlus prior on $\Omega_m = 0.338 \pm 0.018$ with $\theta_{s,d}^{\text{BAO/CMB}}$, $\Omega_m = 0.3 \pm 0.01$, results in an increase in the 1D posterior for h for all models with or without the A_s/n_s prior, as shown in Table II.

The red contours in Fig. 11 show the h vs. Ω_m degeneracy in all four models using FS+BBN+CMBLenS (i.e., no prior on Ω_m). One can see that a negative degeneracy between h and Ω_m is present in all four models we consider. The dashed blue contours show the posterior when we include the PanPlus prior, the solid blue contours further include the CMB-inspired priors on A_s/n_s , and the black contours show the posteriors when PanPlus is replaced with $\theta_{s,d}^{\text{BAO/CMB}}$. One can see that, when the prior on Ω_m decreases, the contours shift along the h/Ω_m degeneracy leading to larger values of h (see the blue vs. black contours in Fig. 11). In addition, this figure clearly shows how the inclusion of the A_s/n_s prior significantly reduces the range of h for both ΛCDM and Δm_e , but has a much smaller effect for EDE and ΔN_{eff} (see the dashed blue vs. solid blue contours in Fig. 11).

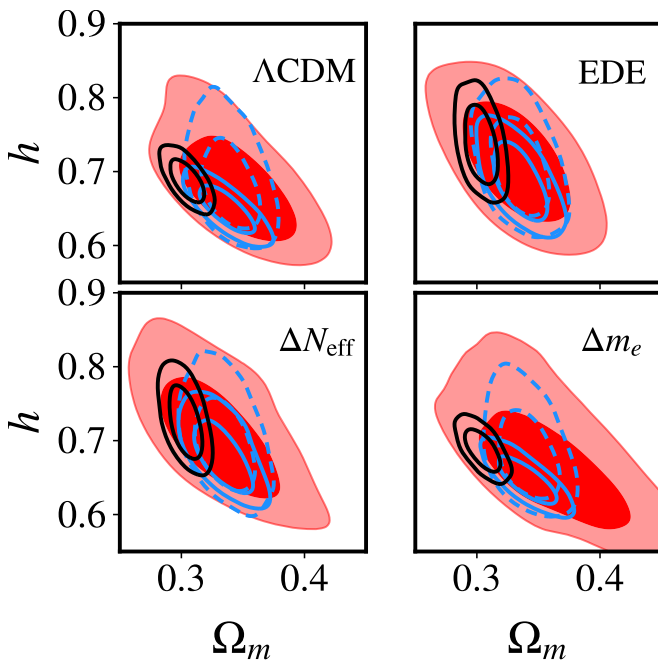


FIG. 11. The h vs. Ω_m degeneracy r_s -marginalized analyses. The filled red contours show constraints using FS+BBN+CMBLenS (i.e., without a prior on Ω_m). The open dashed blue contours show the constraints when we include the PanPlus prior on Ω_m and the open solid blue contours add the effects of the CMB-inspired priors on A_s and n_s . The black contours show the constraints when we keep the priors on A_s and n_s but replace the PanPlus prior with the one from the uncalibrated BAO and CMB measurements of the projected sound horizon.

Note that in our analysis we fixed the sum of the masses of the neutrinos to their minimum value (0.06

eV). We expect that also allowing the neutrino mass to vary, as done in Ref. [31], would make the constraints on h even weaker.

VI. CONCLUSIONS

Full-shape information from measurements of galaxy clustering are poised to contribute important cosmological information when investigating beyond ΛCDM models. Therefore it is important to clarify what aspects of these measurements are driving the constraints.

The constraining power on h predominately comes from the BAO sensitivity to the sound horizon, and the same is true of measurements of the CMB. This has led to the development of a number of beyond- ΛCDM models which change the value of the sound horizon in order to address the Hubble tension. In order to further test these models, it is of interest to develop new analysis methods that extract information about h from observations which are based on pre-recombination physics without relying on the value of the sound horizon.

The full-shape analysis of measured galaxy power spectra can provide such a data set [30]. By marginalizing over the sound horizon and using a BBN prior on ω_b , SNeIa prior on Ω_m , and the measured CMB lensing from *Planck*, the inference of h relies on the amplitude and broad-band shape of the small-scale power spectrum. Previous work has focused on the sensitivity of these data to $k_{\text{eq}} = \Omega_m h$, along with a SNeIa-inspired prior on Ω_m , as the main source of sensitivity to h . Here we have demonstrated that the sensitivity is also driven by the amplitude of the small-scale power spectrum. As a result, beyond- ΛCDM models which are degenerate with A_s/n_s have the ability to affect the r_s -free value of h .

This also has potential implications for using the extended BAO parameter set presented in Ref. [56] and known as ‘ShapeFit’. In this approach, the standard BAO and redshift space distortion parameters are augmented with a parameter that measures the slope of the galaxy power spectrum at $k_{\text{slope}} = 0.03h\text{Mpc}^{-1}$. It has been shown that this extended parameter set is competitive with full-shape analysis of ΛCDM [76]. Since we show here that constraints to the amplitude of the galaxy power spectrum play an important role when considering beyond- ΛCDM models, it will be interesting to check whether ShapeFit will be able to capture some of the important effects of these models.

We find that beyond- ΛCDM models which introduce additional energy density with significant pressure support lead to increased values of h in an r_s -independent analysis. This is due to the ways in which these models suppress the growth of structure and are therefore degenerate with the amplitude of the clustering. Since the amplitude of the small-scale galaxy power spectrum and lensing potential power spectrum play a central role in determining the r_s -free value of h , models which attempt to address both the Hubble and S_8 tensions through a

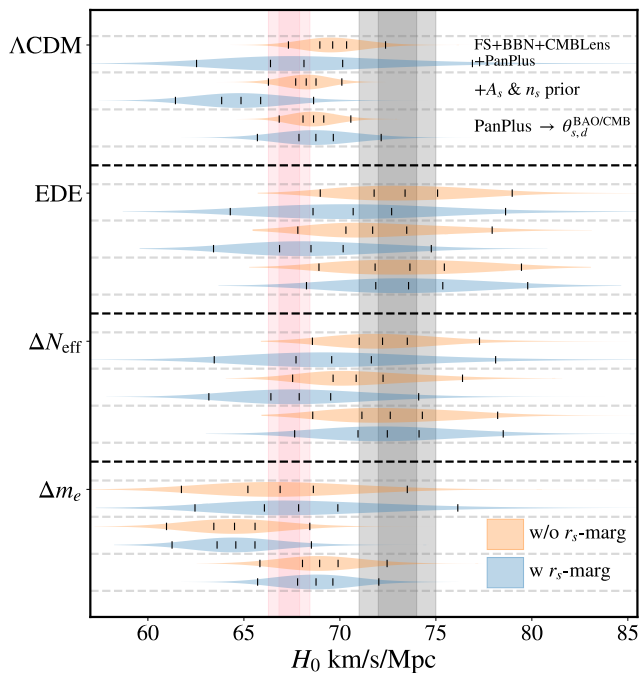


FIG. 12. A full summary of our results. The orange/blue posteriors show the results with/without marginalizing over $r_{s,d}$. For each cosmological model we show analyses with three different choices of priors. We also show the *Planck* constraint to H_0 as the vertical pink band and the SH_0ES constraint in the gray band.

suppression of small-scale power [77–79] may be particularly interesting to consider in light of the analysis presented here.

We have also explored how various priors on cosmological parameters affect these conclusions. When using a CMB-inspired prior on A_s and n_s we found that the model-dependence of these results are even more stark, with EDE and ΔN_{eff} giving posteriors for h which are $\sim 1\sigma$ larger than in ΛCDM . However, the Δm_e model, which only affects recombination, has a posterior for h that is statistically identical to the result in ΛCDM . Additionally, we have emphasized the role played by the Pantheon+ prior on Ω_m in driving the low- h constraints. Replacing the Pantheon+ prior on $\Omega_m = 0.338 \pm 0.018$ with one from the uncalibrated BAO and CMB measurements of the projected sound horizon, $\Omega_m = 0.30 \pm 0.01$, leads to a shift to higher values of h for all models, with EDE and ΔN_{eff} still $\sim 1\sigma$ larger than ΛCDM . The posteriors for h are listed in Tab. II.

We conclude that the Hubble constant inferred from these data depends on both the model and the choice of priors on the cosmological parameters.

Our analysis also allows us to determine whether a comparison between the H_0 posteriors with and without marginalizing over $r_{s,d}$ in ΛCDM provides a robust internal consistency test for physics beyond ΛCDM . A summary of these results is shown in Fig. 12. Using FS+BBN+CMB+PanPlus, one can see that with-

out any prior on A_s and n_s , the agreement in ΛCDM is better than 1σ . The agreement is slightly worse ($\sim 2-2.5\sigma$) once the A_s and n_s priors are included, with a shift in the means of $\Delta H_0 \sim 3\text{km/s/Mpc}$.⁹ Keeping the A_s/n_s prior and changing the Ω_m prior to the uncalibrated BAO and CMB measurements of the projected sound horizon brings the H_0 -values back into excellent agreement.

Given these results, at a minimum we conclude that the consistency of H_0 with and without $r_{s,d}$ -marginalization in ΛCDM depends on the choice of priors on the cosmological parameters. In addition, when the ΛCDM posteriors are consistent, we do not find any indication that the beyond- ΛCDM models are in tension with the data. Given this, our results indicate that with current data the internal consistency test proposed in Refs. [28, 31] is inconclusive.

The results presented here complement those that are presented in Ref. [53]. There we show that the BOSS full-shape analysis using both PyBird and CLASS-PT do not rule out the EDE resolution to the Hubble tension. In light of Ref. [66], it will be useful to perform an analysis similar to what we have done here but using PyBird, since this code relies on a different choice of EFT priors and BOSS power-spectrum measurements. Indeed, the constraints from these two codes may differ up to $\sim 1\sigma$ for ΛCDM due (mostly) to the impact of priors [66]. However, we do not expect the overall conclusions to change, as we have identified physical effects at play in driving degeneracies between h and other parameters.

Current galaxy clustering measurements are not precise enough to rule out or favor beyond ΛCDM models which address the Hubble tension. However, unlike CMB lensing [29], there are several near-future galaxy surveys which will significantly improve constraints on h independent of the sound horizon upon BOSS DR12 (e.g., DESI [80], Euclid [81], VRO [82]). The work presented here highlights the ways in which beyond- ΛCDM models which address the Hubble tension may affect the value of h even in an r_s -free analyses.

ACKNOWLEDGMENTS

We thank Pierre Zhang for contributions at early stages of this work, and his comments and insights throughout the project, Adam Riess, Jose Bernal and Blake Sherwin for helpful comments on the draft, and Eric Jensen and Gerrit Farren for useful conversations. We thank Antony Lewis for help with `getdist`, Oliver Philcox for help with CLASS-PT, and Adam Riess for providing us with the Pantheon+ likelihood. This work used the Strelka Computing Cluster, which is run by

⁹ Using the same priors on n_s and the sum of the neutrino masses as in Ref. [31] we find a similar result, where without (with) marginalizing over $r_{s,d}$, $h = 0.682^{+0.011}_{-0.012}$ ($h = 0.652^{+0.022}_{-0.026}$)

Swarthmore College. TLS is supported by NSF Grant No. 2009377, NASA Grant No. 80NSSC18K0728, and the Research Corporation. This project has received support from the European Union's Horizon 2020 research and innovation program under the Marie Skłodowska-Curie grant agreement No 860881-HIDDeN.

Appendix A: Derivation of the Λ CDM parameter scaling equations

1. Approximate scalings for the galaxy power spectrum

It is helpful to recall the basic physics that determines the small-scale ($k > k_{\text{eq}}$) form of the matter power spectrum. Roughly speaking, dark matter modes with $k > k_{\text{eq}}$ enter the horizon during radiation domination and experience a large Hubble friction, significantly limiting their growth. Once the universe becomes matter dominated all of those modes are able to collapse, growing proportional to a/a_{eq} . This scaling gets modified in detail since the dark matter perturbations do grow logarithmically with scale factor during radiation domination [83], giving an amplitude of the galaxy power spectrum

$$\begin{aligned} P_{\text{gal}}(k > k_{\text{eq}}) &\propto b^2 R_c^2 g(z)^2 A_s (a/a_{\text{eq}})^2 & (A1) \\ &\times [1 + \ln(4a_{\text{eq}}/a_k)]^2 \left(\frac{k}{k_p}\right)^{n_s-1} (h/k)^3, \\ &= b^2 f_b \left[\frac{\omega_b}{\omega_{\text{cdm}}}\right] \Omega_m^{0.25} A_s a^2 \Omega_m^2 h^4 & (A2) \\ &\times \left[1 + \ln\left(\frac{4k/h}{\Omega_m h}\right)\right]^2 \left(\frac{k}{k_p}\right)^{n_s-1} (h/k)^3, \end{aligned}$$

where b is the linear galaxy bias, $R_c \equiv \omega_{\text{cdm}}/\omega_m = 1 - \omega_b/\omega_m$ is the baryon suppression [58], horizon crossing occurs when $k = a_k H(a_k)$, $g(z)^2 \propto \Omega_m^{0.25}$ is the growth function at $z \sim 0.3-0.6$, and k_p is the pivot scale (usually chosen to be $k_p = 0.05 \text{ Mpc}^{-1}$). We note that information about the bias comes from redshift space distortions and the use of informative priors. The second line shows the explicit dependence on h in Λ CDM. During radiation domination we have $a_k = 100 \text{ km/s/Mpc}/c\sqrt{\omega_r}h/k$. Using the fact that $a_{\text{eq}} \equiv \omega_r/\omega_m$ we can write $a_{\text{eq}}/a_k \simeq k/k_{\text{eq}}$. We can see that for $k > k_{\text{eq}}$ the logarithmic term enhances the amplitude. A more careful treatment shows that the logarithmic term is $\ln[k/(8k_{\text{eq}})]$, so for $k_{\text{eq}} \sim 0.01 \text{ hMpc}^{-1}$ and $k_{\text{max}} = 0.4 \text{ hMpc}^{-1}$ we get an enhancement of power at the smallest scales of a factor of ~ 7 [84, 85]. This enhancement gives the sensitivity to k_{eq} .

The correlation of the monopole and quadrupole moments of the galaxy clustering power spectrum gives us redshift space distortion information which provides sensitivity to the product of the growth rate, $f(z)$, and the variance of mass fluctuations in spheres of radius

$R = 8 \text{ Mpc}h^{-1}$ (σ_8^2). First, from Ref. [86] we have

$$\sigma_8^2 \propto A_s (a/a_{\text{eq}})^2 \Omega_m^{0.25} (k_{\text{eq}} h^{-1})^{-1.4} \omega_m^{0.45}, \quad (A3)$$

where the dependence on Ω_m comes from the growth function around the BOSS DR12 redshift bins ($z \sim 0.5$). In Λ CDM, the growth rate is approximately [87]

$$f(z \sim 0.5) \propto \Omega_m^{0.6}. \quad (A4)$$

2. Approximate scaling for the lensing potential power spectrum

Since the *Planck* inferred lensing potential power spectrum provides measurements between $8 \leq L \leq 400$ [71], there are two relevant quantities in the CMB lensing: position of the peak $\ell_{\text{peak}}^{\phi\phi}$ and the amplitude of high L power spectrum, $L^4 C_L^{\phi\phi}$.

First, the peak of the spectrum is set by θ_{eq} at $z \sim 2$ [88], so that $\ell_{\text{peak}}^{\phi\phi} \propto \Omega_m^{0.75} h \omega_r^{-0.5}$.

Second, the CMB lensing potential power spectrum also has sensitivity to k_{eq} . A rough approximation to the combination of parameters measured by estimates of the lensing potential power spectrum is given by [86]

$$L^4 C_L^{\phi\phi} \propto A_s \ell_{\text{eq}}^2 \omega_m^{0.3}, \quad (A5)$$

$$= A_s h^{2.6} \Omega_m^{3.5} \quad (A6)$$

where $\ell_{\text{eq}} \equiv \chi_{\text{dec}} k_{\text{eq}}$, χ_{dec} is the comoving distance to photon decoupling, the power law index for ω_m is fit around $L \simeq 200$, and the primordial power spectrum was taken to be scale invariant. The product $A_s \ell_{\text{eq}}^2$ can be simply understood: the gravitational potential power spectrum is nearly scale invariant up until k_{eq} , at which point it becomes small. The number of collapsed halos of size $r \sim k^{-1}$ that a CMB photon passes by is given by $\chi_*/r \sim k\chi_*$, where χ_* is the comoving distance to the surface of last scattering, and the typical halo potential is $\sim A_s^{1/2}$. Since $\ell_{\text{eq}} = k_{\text{eq}}\chi_*$ gives the largest number of halos along the line of sight, the overall amplitude of the deflection power spectrum (which, in turn, is proportional to the lensing potential power spectrum) is proportional to $A_s \ell_{\text{eq}}^2$ [89]. Additionally, it is straightforward to show that the angular scale of matter radiation equality at the CMB is $\ell_{\text{eq}} \propto \Omega_m^{0.6} h \omega_r^{-0.5}$.

Appendix B: The effect of removing the galaxy power spectrum peak

To demonstrate that the location of the peak of the galaxy power spectrum is not playing a role in constraining h , we performed an analysis with $k_{\text{min}} = 0.05 \text{ hMpc}^{-1}$ for the galaxy power spectrum multipoles. This choice is ~ 5 times larger than k_{eq} , fully removing the peak from the data. The resulting 1D posterior for h is shown in Fig. 13. We can see that the posterior is statistically identical to our fiducial choice of

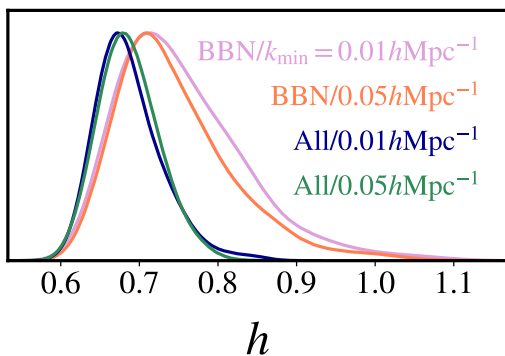


FIG. 13. 1D posterior distribution for h in Λ CDM when marginalizing over $r_{s,d}$ with two different choices for the minimum wavenumber used in the galaxy power spectra multipoles. When using $k_{\min} = 0.05 \text{ hMpc}^{-1}$ we have removed all information about the location of the peak of the galaxy power spectrum. The statistical equivalence for these two values of k_{\min} demonstrates that the location of the peak of the galaxy power spectrum does not play a significant role in constraining h .

$k_{\min} = 0.01 \text{ hMpc}^{-1}$. This is not surprising given the fact that the fiducial k_{\min} is just slightly less than k_{eq} . We note that the signal to noise in the lowest measured modes is smallest since at the largest scales we have the fewest independent measurements.

We note that, although galaxy power spectra may not be able to probe scales large enough to measure the peak, future HI surveys will have enough coverage [57].

Appendix C: Checking the BAO smoothing algorithm

Fig. 5 indicates that part of the parameter space may not be modeled correctly. As discussed in Ref. [90] the BAO smoothing algorithm used in CLASS-PT is constructed to work well for $130 \text{ Mpc} \leq r_{s,d} \leq 170 \text{ Mpc}$. Clearly the Λ CDM MCMCs have samples which are slightly beyond the lower end of this range. The algorithm performs a sine-transform of the matter power spectrum and, excises the BAO bump, interpolates between the two smooth regions on either side, and then inverse transforms back to Fourier space. The excision of the BAO bump is done using fixed boundaries, and so will fail if the BAO bump gets close to either of those boundaries. In order to investigate whether this causes an issue at the lower boundary, we modified the algorithm slightly by allowing the boundary to move as the value of $r_{s,d}$ changes.

Our modified algorithm keeps the distance between the excised points and shifts it linearly with the value of $r_{s,d}$ with the standard value at $r_{s,d} = 150 \text{ Mpc}$. The original algorithm fixes the region of the real-space correlation function that is excised in order to remove the BAO bump. In terms of the indices they remove all points

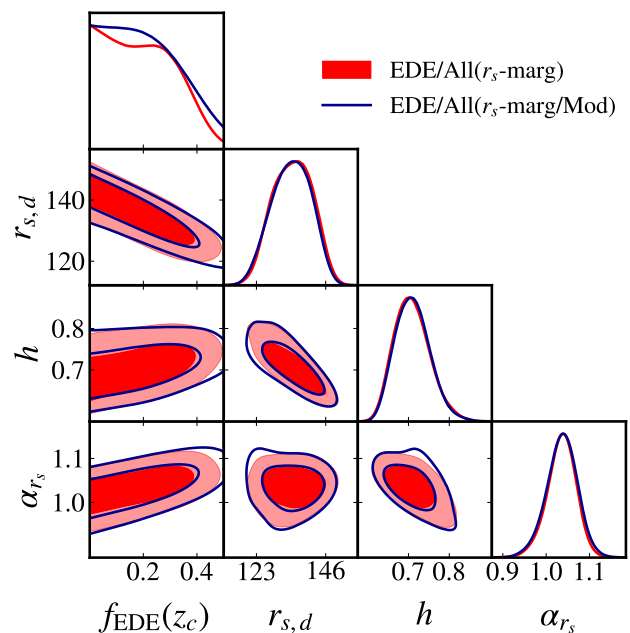


FIG. 14. A triangle plot comparing the posterior distribution between the two smoothing algorithms.

between $N_{\text{left}} = 120$ and $N_{\text{right}} = 240$ [90]. We have modified the range of indices which are removed so that it is translated as the value of $r_{s,d}$ changes:

$$N_{\text{left}} = 120 - 20(1 - r_{s,d}/150)/(1 - 120/150), \quad (\text{C1})$$

and $N_{\text{right}} = N_{\text{left}} + 120$. We have verified that this algorithm properly excises the BAO bump when $r_{s,d}$ is varied between $110 \text{ Mpc} \leq r_{s,d} \leq 170 \text{ Mpc}$.

The comparison between the standard and modified algorithm for EDE is shown in Fig. 14. We focus on EDE here since the value of $r_{s,d}$ has the largest range in this model. There we can see that when ‘All’ of the data is included the two methods are nearly identical. We have checked the other cosmological models we consider show similar insensitivity to the change in the broadband/BAO split.

Appendix D: Verifying the Pantheon+ prior on Ω_m

Instead of using the full Pantheon+ likelihood we have used a prior on $\Omega_m = 0.338 \pm 0.018$. In order to verify that this prior properly captures all of the aspects of this likelihood we have compared the constraints on Λ CDM marginalizing over $r_{s,d}$, using the FS+BBN+CMBLenS+PanPlus, implementing the full Pantheon+ likelihood vs. using the prior on Ω_m .

The comparison between these two analyses is shown in Fig. 15. There we can see that the posteriors are nearly identical, verifying our use of the Pantheon+ prior on Ω_m . The conclusions of this comparison also hold in the

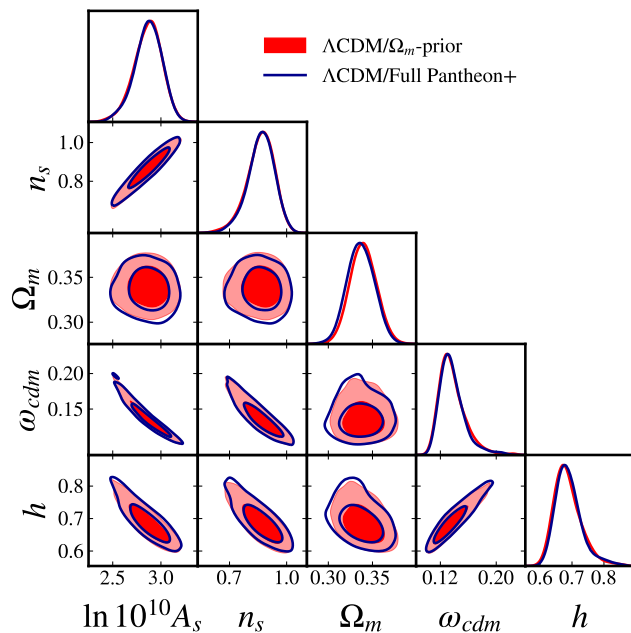


FIG. 15. A triangle plot comparing the posterior distribution between the full Pantheon+ likelihood and a prior on $\Omega_m = 0.338 \pm 0.018$.

beyond- ΛCDM models we consider since they all introduce new physics at or before recombination, and therefore are identical to ΛCDM in the late universe when SNeIa measurements are made.

-
- [1] G. Ellis, The Standard Cosmological Model: Achievements and Issues, *Foundations of Physics* **48**, 1226 (2018).
- [2] P. J. E. Peebles, *Cosmology's Century: An Inside History of Our Modern Understanding of the Universe* (Princeton University Press).
- [3] A. G. Riess *et al.*, A Comprehensive Measurement of the Local Value of the Hubble Constant with $1 \text{ km s}^{-1} \text{ Mpc}^{-1}$ Uncertainty from the Hubble Space Telescope and the SH0ES Team, *ApJ Letters* **934**, L7 (2022), arXiv:2112.04510 [astro-ph.CO].
- [4] N. Aghanim *et al.* (Planck), Planck 2018 results. VI. Cosmological parameters, *Astron. Astrophys.* **641**, A6 (2020), [Erratum: *Astron. Astrophys.* 652, C4 (2021)], arXiv:1807.06209 [astro-ph.CO].
- [5] W. L. Freedman, Measurements of the Hubble Constant: Tensions in Perspective, (2021), arXiv:2106.15656 [astro-ph.CO].
- [6] A. G. Riess *et al.*, A Comprehensive Measurement of the Local Value of the Hubble Constant with 1 km/s/Mpc Uncertainty from the Hubble Space Telescope and the SH0ES Team, (2021), arXiv:2112.04510 [astro-ph.CO].
- [7] E. Abdalla *et al.*, Cosmology intertwined: A review of the particle physics, astrophysics, and cosmology associated with the cosmological tensions and anomalies, *JHEAp* **34**, 49 (2022), arXiv:2203.06142 [astro-ph.CO].
- [8] A. Amon and G. Efstathiou, A non-linear solution to the S_8 tension?, (2022), arXiv:2206.11794 [astro-ph.CO].
- [9] A. Amon *et al.*, Consistent lensing and clustering in a low- S_8 Universe with BOSS, DES Year 3, HSC Year 1 and KiDS-1000, (2022), arXiv:2202.07440 [astro-ph.CO].
- [10] L. Knox and M. Millea, Hubble constant hunter's guide, *Phys. Rev. D* **101**, 043533 (2020), arXiv:1908.03663 [astro-ph.CO].
- [11] E. Di Valentino, O. Mena, S. Pan, L. Visinelli, W. Yang, A. Melchiorri, D. F. Mota, A. G. Riess, and J. Silk, In the realm of the Hubble tension—a review of solutions, *Class. Quant. Grav.* **38**, 153001 (2021), arXiv:2103.01183 [astro-ph.CO].
- [12] N. Schöneberg, G. Franco Abellán, A. Pérez Sánchez, S. J. Witte, V. Poulin, and J. Lesgourgues, The H_0 Olympics: A fair ranking of proposed models, (2021), arXiv:2107.10291 [astro-ph.CO].
- [13] A. G. Riess, L. Breuval, W. Yuan, S. Casertano, L. M. Macri, D. Scolnic, T. Cantat-Gaudin, R. I. Anderson, and M. C. Reyes, Cluster Cepheids with High Precision Gaia Parallaxes, Low Zeropoint Uncertainties, and Hubble Space Telescope Photometry, (2022), arXiv:2208.01045 [astro-ph.CO].
- [14] C. Hikage *et al.* (HSC), Cosmology from cosmic shear power spectra with Subaru Hyper Suprime-Cam first-year data, *Publ. Astron. Soc. Jap.* **71**, 43 (2019), arXiv:1809.09148 [astro-ph.CO].
- [15] C. Heymans *et al.*, KiDS-1000 Cosmology: Multi-probe weak gravitational lensing and spectroscopic galaxy clustering constraints, *Astron. Astrophys.* **646**, A140 (2021), arXiv:2007.15632 [astro-ph.CO].
- [16] T. M. C. Abbott *et al.* (DES), Dark Energy Survey Year 3 Results: Cosmological Constraints from Galaxy Clustering and Weak Lensing, (2021), arXiv:2105.13549 [astro-ph.CO].
- [17] G. E. Addison, Y. Huang, D. J. Watts, C. L. Bennett, M. Halpern, G. Hinshaw, and J. L. Weiland, Quantifying discordance in the 2015 Planck CMB spectrum,

- Astrophys. J. **818**, 132 (2016), arXiv:1511.00055 [astro-ph.CO].
- [18] N. Aghanim *et al.* (Planck), Planck intermediate results. LI. Features in the cosmic microwave background temperature power spectrum and shifts in cosmological parameters, *Astron. Astrophys.* **607**, A95 (2017), arXiv:1608.02487 [astro-ph.CO].
- [19] M. Vonlanthen, S. Räsänen, and R. Durrer, Model-independent cosmological constraints from the CMB, *JCAP* **08**, 023, arXiv:1003.0810 [astro-ph.CO].
- [20] B. Audren, J. Lesgourgues, K. Benabed, and S. Prunet, Conservative Constraints on Early Cosmology: an illustration of the Monte Python cosmological parameter inference code, *JCAP* **02**, 001, arXiv:1210.7183 [astro-ph.CO].
- [21] B. Audren, Separate Constraints on Early and Late Cosmology, *Mon. Not. Roy. Astron. Soc.* **444**, 827 (2014), arXiv:1312.5696 [astro-ph.CO].
- [22] L. Verde, E. Bellini, C. Pigozzo, A. F. Heavens, and R. Jimenez, Early Cosmology Constrained, *JCAP* **04**, 023, arXiv:1611.00376 [astro-ph.CO].
- [23] W. Lin, X. Chen, and K. J. Mack, Early Universe Physics Insensitive and Uncalibrated Cosmic Standards: Constraints on Ω_m and Implications for the Hubble Tension, *Astrophys. J.* **920**, 159 (2021), arXiv:2102.05701 [astro-ph.CO].
- [24] J. L. Bernal, L. Verde, and A. G. Riess, The trouble with H_0 , *JCAP* **10**, 019, arXiv:1607.05617 [astro-ph.CO].
- [25] K. Aylor, M. Joy, L. Knox, M. Millea, S. Raghunathan, and W. L. K. Wu, Sounds Discordant: Classical Distance Ladder & Λ CDM -based Determinations of the Cosmological Sound Horizon, *Astrophys. J.* **874**, 4 (2019), arXiv:1811.00537 [astro-ph.CO].
- [26] G. Benevento, W. Hu, and M. Raveri, Can Late Dark Energy Transitions Raise the Hubble constant?, *Phys. Rev. D* **101**, 103517 (2020), arXiv:2002.11707 [astro-ph.CO].
- [27] G. Efstathiou, To H_0 or not to H_0 ?, *Mon. Not. Roy. Astron. Soc.* **505**, 3866 (2021), arXiv:2103.08723 [astro-ph.CO].
- [28] G. S. Farren, O. H. E. Philcox, and B. D. Sherwin, Determining the Hubble constant without the sound horizon: Perspectives with future galaxy surveys, *Phys. Rev. D* **105**, 063503 (2022), arXiv:2112.10749 [astro-ph.CO].
- [29] E. J. Baxter and B. D. Sherwin, Determining the Hubble Constant without the Sound Horizon Scale: Measurements from CMB Lensing, *Mon. Not. Roy. Astron. Soc.* **501**, 1823 (2021), arXiv:2007.04007 [astro-ph.CO].
- [30] O. H. Philcox, B. D. Sherwin, G. S. Farren, and E. J. Baxter, Determining the Hubble Constant without the Sound Horizon: Measurements from Galaxy Surveys, (2020), arXiv:2008.08084 [astro-ph.CO].
- [31] O. H. E. Philcox, G. S. Farren, B. D. Sherwin, E. J. Baxter, and D. J. Brout, Determining the Hubble Constant without the Sound Horizon: A 3.6% Constraint on H_0 from Galaxy Surveys, CMB Lensing and Supernovae, (2022), arXiv:2204.02984 [astro-ph.CO].
- [32] D. Baumann, A. Nicolis, L. Senatore, and M. Zaldarriaga, Cosmological Non-Linearities as an Effective Fluid, *JCAP* **07**, 051, arXiv:1004.2488 [astro-ph.CO].
- [33] J. J. M. Carrasco, M. P. Hertzberg, and L. Senatore, The Effective Field Theory of Cosmological Large Scale Structures, *JHEP* **09**, 082, arXiv:1206.2926 [astro-ph.CO].
- [34] L. Senatore and M. Zaldarriaga, The IR-resummed Effective Field Theory of Large Scale Structures, *JCAP* **1502** (02), 013, arXiv:1404.5954 [astro-ph.CO].
- [35] L. Senatore, Bias in the Effective Field Theory of Large Scale Structures, *JCAP* **1511** (11), 007, arXiv:1406.7843 [astro-ph.CO].
- [36] L. Senatore and M. Zaldarriaga, Redshift Space Distortions in the Effective Field Theory of Large Scale Structures, (2014), arXiv:1409.1225 [astro-ph.CO].
- [37] A. Perko, L. Senatore, E. Jennings, and R. H. Wechsler, Biased Tracers in Redshift Space in the EFT of Large-Scale Structure, (2016), arXiv:1610.09321 [astro-ph.CO].
- [38] S. Alam *et al.* (BOSS), The clustering of galaxies in the completed SDSS-III Baryon Oscillation Spectroscopic Survey: cosmological analysis of the DR12 galaxy sample, *Mon. Not. Roy. Astron. Soc.* **470**, 2617 (2017), arXiv:1607.03155 [astro-ph.CO].
- [39] G. D'Amico, J. Gleyzes, N. Kokron, D. Markovic, L. Senatore, P. Zhang, F. Beutler, and H. Gil-Marín, The Cosmological Analysis of the SDSS/BOSS data from the Effective Field Theory of Large-Scale Structure, *JCAP* **05**, 005, arXiv:1909.05271 [astro-ph.CO].
- [40] M. M. Ivanov, M. Simonović, and M. Zaldarriaga, Cosmological Parameters from the BOSS Galaxy Power Spectrum, *JCAP* **05**, 042, arXiv:1909.05277 [astro-ph.CO].
- [41] T. Colas, G. D'Amico, L. Senatore, P. Zhang, and F. Beutler, Efficient Cosmological Analysis of the SDSS/BOSS data from the Effective Field Theory of Large-Scale Structure, *JCAP* **06**, 001, arXiv:1909.07951 [astro-ph.CO].
- [42] G. D'Amico, L. Senatore, and P. Zhang, Limits on w CDM from the EFTofLSS with the PyBird code, *JCAP* **01**, 006, arXiv:2003.07956 [astro-ph.CO].
- [43] G. D'Amico, Y. Donath, L. Senatore, and P. Zhang, Limits on Clustering and Smooth Quintessence from the EFTofLSS, (2020), arXiv:2012.07554 [astro-ph.CO].
- [44] S.-F. Chen, Z. Vlah, and M. White, A new analysis of the BOSS survey, including full-shape information and post-reconstruction BAO, (2021), arXiv:2110.05530 [astro-ph.CO].
- [45] P. Zhang, G. D'Amico, L. Senatore, C. Zhao, and Y. Cai, BOSS Correlation Function analysis from the Effective Field Theory of Large-Scale Structure, *JCAP* **02** (02), 036, arXiv:2110.07539 [astro-ph.CO].
- [46] P. Zhang and Y. Cai, BOSS full-shape analysis from the EFTofLSS with exact time dependence, *JCAP* **01** (01), 031, arXiv:2111.05739 [astro-ph.CO].
- [47] O. H. E. Philcox and M. M. Ivanov, BOSS DR12 full-shape cosmology: Λ CDM constraints from the large-scale galaxy power spectrum and bispectrum monopole, *Phys. Rev. D* **105**, 043517 (2022), arXiv:2112.04515 [astro-ph.CO].
- [48] T. Simon, G. Franco Abellán, P. Du, V. Poulin, and Y. Tsai, Constraining decaying dark matter with BOSS data and the effective field theory of large-scale structures, *Phys. Rev. D* **106**, 023516 (2022), arXiv:2203.07440 [astro-ph.CO].
- [49] S. Kumar, R. C. Nunes, and P. Yadav, Updating non-standard neutrinos properties with Planck-CMB data and full-shape analysis of BOSS and eBOSS galaxies, (2022), arXiv:2205.04292 [astro-ph.CO].
- [50] R. C. Nunes, S. Vagnozzi, S. Kumar, E. Di Valentino, and O. Mena, New tests of dark sector interactions from the full-shape galaxy power spectrum, *Phys. Rev. D* **105**, 123506 (2022), arXiv:2203.08093 [astro-ph.CO].

- [51] A. Laguë, J. R. Bond, R. Hložek, K. K. Rogers, D. J. E. Marsh, and D. Grin, Constraining Ultralight Axions with Galaxy Surveys, (2021), arXiv:2104.07802 [astro-ph.CO].
- [52] P. Carrilho, C. Moretti, and A. Pourtsidou, Cosmology with the EFTofLSS and BOSS: dark energy constraints and a note on priors, (2022), arXiv:2207.14784 [astro-ph.CO].
- [53] T. Simon, P. Zhang, V. Poulin, and T. L. Smith, Updated constraints from the effective field theory analysis of BOSS power spectrum on Early Dark Energy, (2022), arXiv:2208.05930 [astro-ph.CO].
- [54] D. Brout *et al.*, The Pantheon+ Analysis: Cosmological Constraints, (2022), arXiv:2202.04077 [astro-ph.CO].
- [55] P. A. R. Ade *et al.* (Planck), Planck 2013 results. XVI. Cosmological parameters, *Astron. Astrophys.* **571**, A16 (2014), arXiv:1303.5076 [astro-ph.CO].
- [56] S. Brieden, H. Gil-Marín, and L. Verde, ShapeFit: extracting the power spectrum shape information in galaxy surveys beyond BAO and RSD, *JCAP* **12** (12), 054, arXiv:2106.07641 [astro-ph.CO].
- [57] S. Cunningham, Detecting the power spectrum turnover with H I intensity mapping, *Mon. Not. Roy. Astron. Soc.* **512**, 2408 (2022), arXiv:2202.13828 [astro-ph.CO].
- [58] J. L. Bernal, T. L. Smith, K. K. Boddy, and M. Kamionkowski, Robustness of baryon acoustic oscillations constraints to beyond- Λ CDM cosmologies, (2020), arXiv:2004.07263 [astro-ph.CO].
- [59] V. Poulin, T. L. Smith, T. Karwal, and M. Kamionkowski, Early Dark Energy Can Resolve The Hubble Tension, *Phys. Rev. Lett.* **122**, 221301 (2019), arXiv:1811.04083.
- [60] T. L. Smith, V. Poulin, and M. A. Amin, Oscillating scalar fields and the Hubble tension: a resolution with novel signatures, *Phys. Rev. D* **101**, 063523 (2020), arXiv:1908.06995 [astro-ph.CO].
- [61] L. Hart and J. Chluba, New constraints on time-dependent variations of fundamental constants using Planck data, *Mon. Not. Roy. Astron. Soc.* **474**, 1850 (2018), arXiv:1705.03925 [astro-ph.CO].
- [62] L. Hart and J. Chluba, Varying fundamental constants principal component analysis: additional hints about the Hubble tension, *Mon. Not. Roy. Astron. Soc.* **510**, 2206 (2022), arXiv:2107.12465 [astro-ph.CO].
- [63] T. Brinckmann and J. Lesgourgues, MontePython 3: boosted MCMC sampler and other features, (2018), arXiv:1804.07261 [astro-ph.CO].
- [64] D. Blas, J. Lesgourgues, and T. Tram, The Cosmic Linear Anisotropy Solving System (CLASS) II: Approximation schemes, *JCAP* **1107**, 034, arXiv:1104.2933 [astro-ph.CO].
- [65] S. Alam *et al.*, The Eleventh and Twelfth Data Releases of the Sloan Digital Sky Survey: Final Data from SDSS-III, *ApJ Supplemental* **219**, 12 (2015), arXiv:1501.00963 [astro-ph.IM].
- [66] T. Simon, P. Zhang, V. Poulin, and T. L. Smith, On the consistency of effective field theory analyses of BOSS power spectrum, (2022), arXiv:2208.05929 [astro-ph.CO].
- [67] N. Schöneberg, J. Lesgourgues, and D. C. Hooper, The BAO+BBN take on the hubble tension, *Journal of Cosmology and Astroparticle Physics* **2019** (10), 029.
- [68] R. Consiglio, P. de Salas, G. Mangano, G. Miele, S. Pastor, and O. Pisanti, PArthENoPE reloaded, *Computer Physics Communications* **233**, 237 (2018). arXiv:1808.07317 [astro-ph.CO].
- [69] 10.3847/1538-4357/aaab53 (2018).
- [70] E. Aver, K. A. Olive, and E. D. Skillman, The effects of he i λ 10830 on helium abundance determinations, *Journal of Cosmology and Astroparticle Physics* **2015** (07), 011.
- [71] N. Aghanim *et al.* (Planck), Planck 2018 results. VIII. Gravitational lensing, *Astron. Astrophys.* **641**, A8 (2020), arXiv:1807.06210 [astro-ph.CO].
- [72] G. Ye, B. Hu, and Y.-S. Piao, Implication of the Hubble tension for the primordial Universe in light of recent cosmological data, *Phys. Rev. D* **104**, 063510 (2021), arXiv:2103.09729 [astro-ph.CO].
- [73] D. Aloni, A. Berlin, M. Joseph, M. Schmaltz, and N. Weiner, A Step in Understanding the Hubble Tension, (2021), arXiv:2111.00014 [astro-ph.CO].
- [74] A. Gelman and D. B. Rubin, Inference from Iterative Simulation Using Multiple Sequences, *Statist. Sci.* **7**, 457 (1992).
- [75] A. Lewis, GetDist: a Python package for analysing Monte Carlo samples, (2019), arXiv:1910.13970 [astro-ph.IM].
- [76] S. Brieden, H. Gil-Marín, and L. Verde, Model-agnostic interpretation of 10 billion years of cosmic evolution traced by BOSS and eBOSS data, (2022), arXiv:2204.11868 [astro-ph.CO].
- [77] I. J. Allali, M. P. Hertzberg, and F. Rompineve, A Dark Sector to Restore Cosmological Concordance, (2021), arXiv:2104.12798 [astro-ph.CO].
- [78] S. J. Clark, K. Vattis, J. Fan, and S. M. Koushiappas, The H_0 and S_8 tensions necessitate early and late time changes to Λ CDM, (2021), arXiv:2110.09562 [astro-ph.CO].
- [79] M. Joseph, D. Aloni, M. Schmaltz, E. N. Sivarajan, and N. Weiner, A Step in Understanding the S_8 Tension, (2022), arXiv:2207.03500 [astro-ph.CO].
- [80] A. Aghamousa *et al.* (DESI), The DESI Experiment Part I: Science, Targeting, and Survey Design, (2016), arXiv:1611.00036 [astro-ph.IM].
- [81] R. Laureijs *et al.* (EUCLID), Euclid Definition Study Report, (2011), arXiv:1110.3193 [astro-ph.CO].
- [82] LSST Science Collaboration, LSST Science Book, Version 2.0, arXiv e-prints, arXiv:0912.0201 (2009), arXiv:0912.0201 [astro-ph.IM].
- [83] P. Meszaros, The behaviour of point masses in an expanding cosmological substratum., *A&A* **37**, 225 (1974).
- [84] D. J. Eisenstein and W. Hu, Baryonic features in the matter transfer function, *Astrophys. J.* **496**, 605 (1998), arXiv:astro-ph/9709112.
- [85] S. Dodelson, *Modern Cosmology* (Academic Press, Amsterdam, 2003).
- [86] P. A. R. Ade *et al.* (Planck), Planck 2015 results. XV. Gravitational lensing, *Astron. Astrophys.* **594**, A15 (2016), arXiv:1502.01591 [astro-ph.CO].
- [87] S. M. Carroll, W. H. Press, and E. L. Turner, The cosmological constant., *Ann. Rev. Astron. & Astrophys.* **30**, 499 (1992).
- [88] A. Lewis and A. Challinor, Weak gravitational lensing of the CMB, *Phys. Rept.* **429**, 1 (2006), arXiv:astro-ph/0601594.
- [89] D. Hanson, A. Challinor, and A. Lewis, Weak lensing of the CMB, *General Relativity and Gravitation* **42**, 2197 (2010), arXiv:0911.0612 [astro-ph.CO].
- [90] A. Chudaykin, M. M. Ivanov, O. H. E. Philcox, and M. Simonović, Nonlinear perturbation theory extension of the Boltzmann code CLASS, *Phys. Rev. D* **102**, 063533 (2020), arXiv:1908.07317 [astro-ph.CO].

(2020), arXiv:2004.10607 [astro-ph.CO].